Polymer Testing 55 (2016) 297–309

Contents lists available at ScienceDirect

Polymer Testing

journal homepage: www.elsevier.com/locate/polytest

Test Method

# Structural versus microstructural evolution of semi-crystalline polymers during necking under tension: Influence of the skin-core effects, the relative humidity and the strain rate

Lucien Laiarinandrasana [a, *], Nathan Selles [a], Olga Klinkova [a], Thilo F. Morgeneyer [a], Henry Proudhon [a], Lukas Helfen [b, c]

[a] PSL-Research University, MINES ParisTech, Centre des Matériaux, CNRS UMR7633, BP 87, F-91003 Evry Cedex, France
[b] European Synchrotron Radiation Facility, BP 220, 38043 Grenoble Cedex, France
[c] ANKA Karlsruhe Institute of Technology (KIT), D-76344 Eggenstein-Leopoldshafen, Germany

ARTICLE INFO

*Article history:*
Received 4 August 2016
Accepted 12 September 2016
Available online 13 September 2016

*Keywords:*
Semi-crystalline polymers
X-ray tomography
Void anisotropy
Tensile test
Necking

ABSTRACT

This study deals with the appearance of heterogeneity of strain and stress in a uniaxial specimen deformed by extension. For this purpose, two semi-crystalline polymers (an isotactic polypropylene and a polyamide 6), were selected: flat geometries showing a marked microstructural skin-core effect for the PP and homogeneous round bars for PA6 which were systematically compared during tensile loading. The specimens underwent necking at various strain rates and two relative humidities. The minimum neck curvature radius and the net section area decreased at high strain rates and low relative humidity (dried samples). The gradual localization of the deformation by the necking process was analysed by inspecting the changes in the microstructure. Tomography allowed the observations of voids appearing within spherulites in the form of two symmetrical fans, one at each end of the spherulites. A full study of these polar fans has been carried out in terms of morphology, general arrangement and characteristic length. The latter allowed axial and transverse deformations to be experimentally measured at the scale of the individual voids, the polar fans and the spherulites. The strain distributions were plotted with respect to the axial and radial directions. Heterogeneous strains were found: i) to be due to the necking for the two materials; ii) and due to the initial skin-core effects in the PP. These heterogeneities imply that the evolution of the volume variation of the specimen by measurement at the surface could not accurately reflect through-volume effects, as the assumptions of isotropy and homogeneity are not satisfied. Experimental data derived from uniaxial tensile tests should be enriched to build relevant constitutive models.



## 1. Introduction

Weight saving for engineering structures constitutes one of the motivations promoting the use of organic materials for the replacement of metals. This usually requires the redesign of industrial components in order to comply with their safety in use. Amongst the large range of structural polymers, thermoplastics have gained increasing interest thanks to their lower fabrication costs. Indeed, pre-designed shapes can be processed very close to their final complex profiles. Designing such complex shapes needs numerical computation generally based on finite element (FE) codes, relying on constitutive models based on the true stress-strain curve.

Traditionally, uniaxial tensile tests have been the principal means of obtaining the engineering stresses and strains of the materials under load. Since the true stress-strain curve is derived from engineering stress-strain plot using transverse properties (Section 2: **Theory**), the development of VideoTraction [1] and full field measurement combined with digital image correlation (DIC) improved knowledge of the mechanical behaviour of a given material. However, these strain 2D data still lack through-thickness information. To overcome this difficulty, it is generally admitted that:

* Corresponding author.
*E-mail address:* Lucien.laiarinandrasana@mines-paristech.fr (L. Laiarinandrasana).

http://dx.doi.org/10.1016/j.polymertesting.2016.09.012
0142-9418/

- the stress and the strain are homogeneously distributed within the gauge length of the tested specimen;
- by isotropy, the out of plane deformation is similar to that measured transversely.

This work aims at checking experimentally the validity of assumptions of isotropy and homogeneity, using an approach based on the relation between evolution of the microstructure during deformation and the mechanical properties. To this end, Section 3 details the specimens and the spherulitic microstructure of the two semi-crystalline polymers under study: an isotactic polypropylene (PP) and a polyamide 6 (PA6). These specimens were subjected to tensile tests with specific strain rates and preconditioning so as to provoke necking during the test. Experimental data during the necking process were collected, allowing the identification of the stage in the stress-strain curve where the minimum neck curvature radius was reached. This change in the shape of the specimen highlights, at the macroscopic scale, heterogeneity induced by the deformation. The last part of section 3 attempts to reveal the heterogeneity at the microscopic scale. To this end, necked specimens were produced so as to collect comprehensive through-thickness data in 3D from the deformed microstructures and, further, to depict their evolution. Unlike observation techniques such as SAXS, WAXS [2,3] and IPSLT [4] used to investigate such information on semi-crystalline polymers, synchrotron radiation computed tomography (SRCT) [5–7] has been used here. At a resolution of about 0.7 μm, the heights and the diameters of microstructural patterns such as individual voids and cluster of voids arranged into polar fans could be evaluated. From these SRCT data, the deviation from the homogeneity assumption could be analysed.

Section 4 sets three points of discussion: i) the outcome of the through thickness SRCT data in comparison with traditional measurements at the surface (load, full-field displacement); ii) the determination of the local strains that can be split into shear and volumetric parts; iii) the consequence of a better understanding of the link between microstructural evolution and macroscopic mechanical properties on the FE constitutive models.

## 2. Theory

Engineering stress-strain curves are obtained experimentally but constitutive modelling requires the true stress versus true strain curve to be correctly integrated. Let (r, θ, z) be the cylindrical coordinates where the load applied to the tensile specimen is in the z direction (Fig. 1).

Consider a representative volume element (RVE) where the stress and strain are supposed to be homogeneous. In Appendix A, it is shown that calculation of the true strain is straightforward, by integrating the increment of strain.

$$\varepsilon_z = ln\left[1 + \frac{\Delta l_z}{l_z^0}\right] \tag{1}$$

where $l_z$ is the actual length $l$ in the $z$ direction and $l_z^0$ is the initial value of $l_z$.

The true stress is a function of the transverse strains $\varepsilon_r$ and $\varepsilon_\theta$ (Appendix A):

$$\sigma_z = \frac{F}{S} = \frac{F}{S_0} e^{-(\varepsilon_r + \varepsilon_\theta)} \tag{2}$$

where $F$ is the tensile load $S_0$ and $S$ are the initial and actual section areas, respectively. Assuming that the material is both isotropic and isochoric (incompressible), the classical relationship between the engineering stress $F/S_0$ and the true stress can be derived from Eq. (2), so that:

$$\sigma_z = \frac{F}{S_0}\left(1 + \frac{\Delta l_z}{l_z^0}\right) \tag{3}$$

In the present work, the polymers under investigation were considered to be isotropic, at least initially, but not isochoric. Indeed, in contrast to metals in the plastic regime, polymeric materials are known to be pressure sensitive [1,9–13] due to volume changes. Therefore, the calculation of the true stress should be performed using Eq. (2). A partial answer can be given by full field strain measurement obtained by Digital Image Correlation (DIC). Indeed, $\varepsilon_r$ and $\varepsilon_\theta$ were also measured *at the surface* during the deformation. However, there was no guarantee that these transverse deformations were homogeneous throughout the thickness, especially on samples with pre-existing skin-core effects.

Moreover, when the specimen underwent necking, the applied load together with the material response induce heterogeneity inside the necked zone. For notched round bars, the Bridgman formulae reported in Appendix A might be more relevant to describe the multiaxial stress state within the net section [8,14]:

$$\begin{aligned} \sigma_z(r) &= \sigma_{eq}\left[1 + ln\left(1 + \frac{a^2 - r^2}{2aR}\right)\right] \\ \sigma_r(r) = \sigma_\theta(r) &= \sigma_{eq}\left[ln\left(1 + \frac{a^2 - r^2}{2aR}\right)\right] \end{aligned} \tag{4}$$

where: $a$ is the net section radius, $R$ is the neck curvature radius and $\sigma_{eq}$ is the Von Mises equivalent stress.

Note that the principal stresses in Eq. (4) depend on the geometrical parameters $a$ and $R$. Measuring their current values during the stretching of the sample allowed estimation of the multiaxial true stress state within the net section of the material.

## 3. Materials and methods

### 3.1. Materials and specimens

#### 3.1.1. Polypropylene and polyamide 6 semi-crystalline polymers

Two semi-crystalline polymers have been considered in this study: an isotactic polypropylene (PP) and a polyamide 6 (PA6) [6,17,18]. The glass transition temperatures $T_g$ and the degrees of crystallinity of the two materials, evaluated using modulated differential scanning calorimetry are given in Table 1. The pronounced dependence of $T_g$ on the water content was studied and summarized in Table 2.

#### 3.1.2. Specimens

For PP, ISO flat dumbbell specimens were provided after injection moulding. The gauge length $l_z^0$ was equal to 25 mm (Fig. 1a).

Optical microscope observations on microtomed slices of the rectangular section in Fig. 2a showed increasing sperulite diameter from the surface (skin) towards the core of the sample. Some quasi-parabolic spherulites [15] were observed at the interface between the skin and the core, due to the thermal gradient during crystallization [16]. Fig. 2b illustrates the regular spherulites in the core. Their diameter is fairly homogeneous with an average value of about 60 μm. This change in both morphology and size of spherulites through the thickness is defined here as the skin-core effect.

For PA6, the 10 mm thick plate also exhibited skin-core effects [6]. However, machined round bars extracted from mid-thickness of this plate allowed homogeneous equi-axed spherulites to be obtained. The characteristic lengths of these round bars are given in

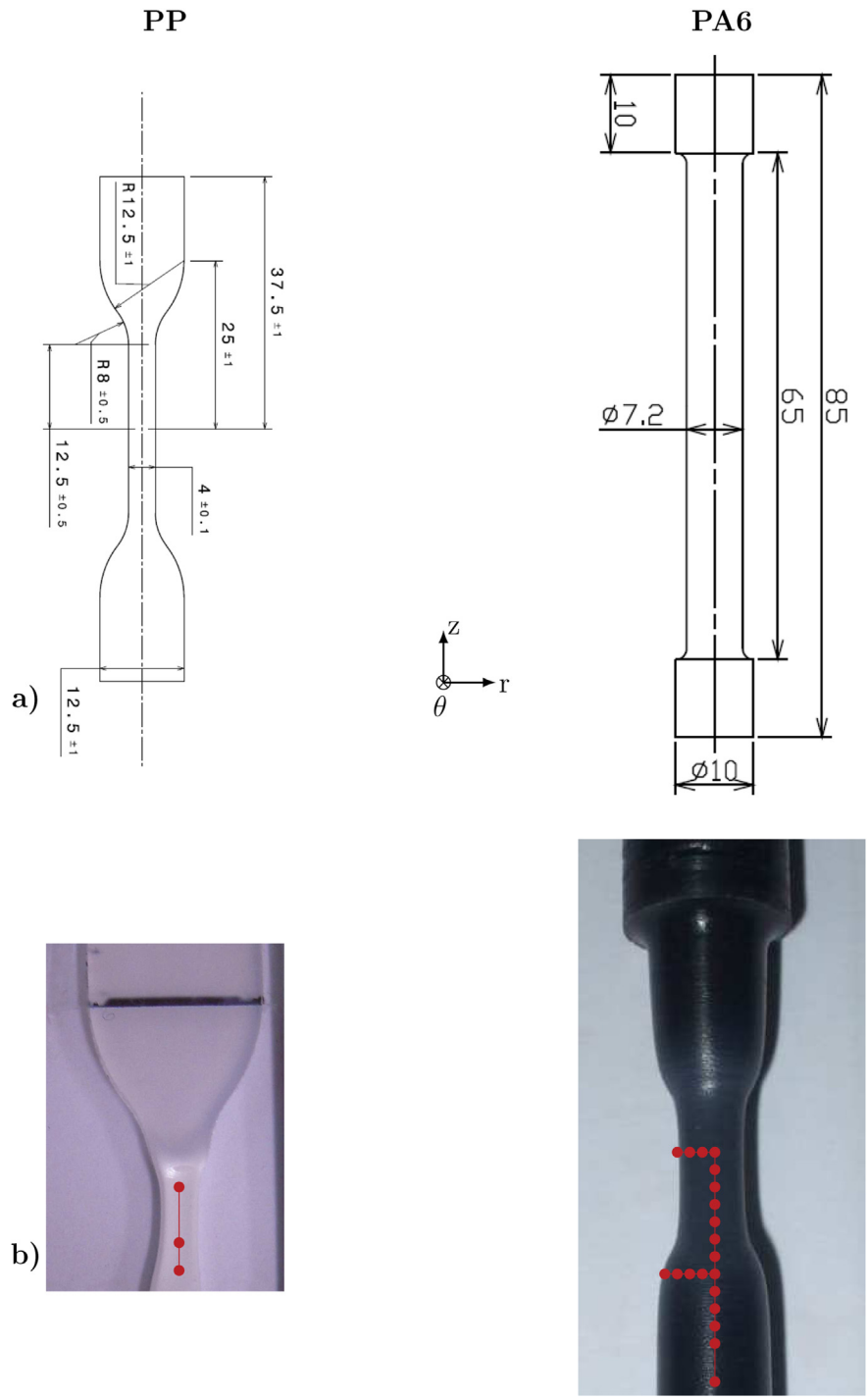


**Fig. 1.** Tensile test specimens for PP (left) and PA6 (right): a) PP flat specimen NF EN ISO 527-2, thickness = (2 ± 0.1) mm and b) PA6 round bar ASTM D638-91 and D2990; b). Pictures of necked samples with the locations of tomography scans. (*All dimensions in mm*).

**Table 1**
Glass transition temperature (**$T_g$**) and degree of crystallinity ($X$) for the isotactic polypropylene (PP) and polyamide 6 (PA6) measured using MDSC technique.

| Material | $T_g$ (°C) | $X$(%) |
|---|---|---|
| PP | −8 | 53 |
| PA6 (RH = 0) | 47 | 43 |

**Table 2**
Water uptake and glass transition temperature (**$T_g$**) of the PA6 in function of the relative humidity RH.

| RH (%) | Water uptake (%) | $T_g$ (°C) |
|---|---|---|
| 0 | 0 | 53 |
| 50 | 1.8 | 4 |
| 100 | 5.8 | −25 |

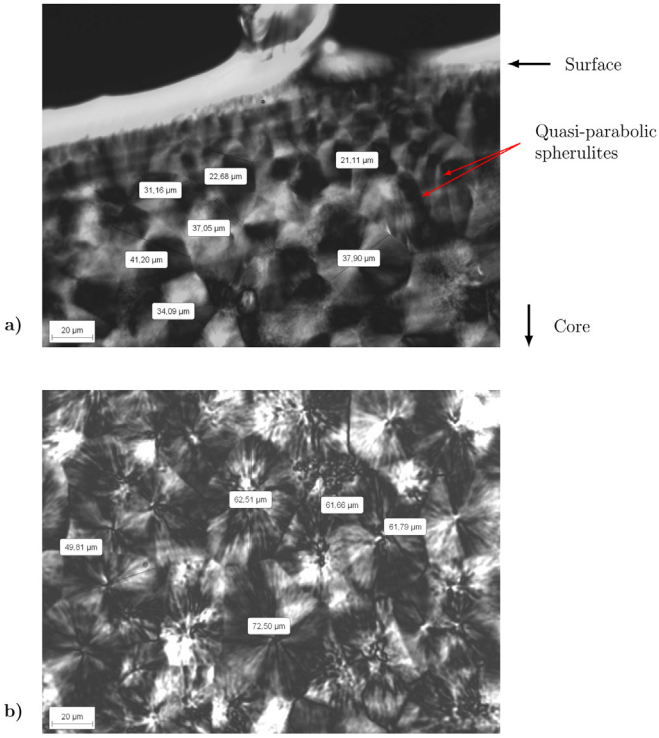


**Fig. 2.** Microscopic observations of the skin-core effects on spherulitic microstructures of PP: a) Skin; b) Core.

Fig. 1a, where $l_z^0 = 65$ mm.

### 3.2. Experiments

#### 3.2.1. Tensile tests conditions to characterize necking

Tensile tests were carried out using an electromechanical tensile rig at various crosshead speeds, at a controlled test temperature of 20 °C and relative humidity (RH) of 50%. The PP specimens were stored in the test room before test, with no specific pre-conditioning. As the PA6 material was known to be hydrophilic, two pre-conditioning procedures were applied. The first consisted of specimens that were dried, stored in a dessicator and then immediately exposed to the test conditions (20 °C and RH = 50%) and tested. They are labelled RH0 in the following. The second series of PA6 specimens were stored in the same test room as the PP specimens. They are referenced as RH50 specimens.

The experimental procedure consisted of first carrying out a tensile test up to failure of the specimen. This aimed at checking if the test conditions (strain rate and pre-conditioning) allowed the appearance of necking during deformation. The experimental setup was equipped with a DC camera for DIC purposes. The images were synchronized with the engineering strain and stress so as to follow the evolution of the neck characteristic lengths ($a$ and $R$). Next, a series of tests were stopped when a substantial neck extension was observed at the macroscopic scale. Note that, for the PP flat samples, '$a$', stands specifically for the half width of the specimen. No macroscopic measurement of the evolution of the thickness was performed. The engineering strain rate ranged from $4.10^{-4}$ $s^{-1}$ to $10^{-2}$ $s^{-1}$ for PP and from 3.5 $10^{-3}$ $s^{-1}$ to $10^{-2}$ $s^{-1}$ for PA6.

#### 3.2.2. Tomography observations of the necked regions

For the specimens where $a$ and $R$ were measured during the necking process, an attempt was made to examine the evolution of the microstructue around the necked region. To this end, inspections of the PP and PA6 necked samples (Fig. 1b) were performed at the imaging beamline ID19 of the European Synchrotron Radiation Facility (Grenoble, France). For the SRCT experiments [6,19], the pink beam of a single-line undulator with a photon energy of approximately ~19 keV was used. Using a 20 µm thick GGG scintillator coupled via refractive microscope optics [20] to a 2D pixel array detector based on a charge-coupled device, 1500 projections for each scan with an executive pixel size of 0.7 µm were recorded. Reconstruction of 3D volume data was performed slice-by-slice using an accelerated filtered-back projection algorithm [21]. As depicted in Fig. 1b left, along the $z$-axis, a series of 3 scans was obtained, consisting each of a volume of $(1433\ \mu m)^3$. The three aligned red dots correspond each to one data set.

The PA6 necked specimens were studied using 19 scans (red dots) with 3D data sizes of $(716 \times 716 \times 358)\ \mu m^3$ each, composed of (Fig. 1b right):

- 12 scans aligned along the $z$-axis from the nominal diameter to the necked zone;
- 3 scans radially inside the necked zone;
- 4 scans radially around the neck shoulder.

## 4. Results

For the sake of comparison, the figures in this paper have generally been presented such that the left column shows data for PP and the right column for PA6. The label of each column is set in the upper part of the figure.

### 4.1. Tensile tests

Fig. 3a summarizes the trends of the engineering stress strain curves. Only a few of them are shown, for reasons of clarity, so as to show the strain rate effects. For a given conditioning, the usual trend was observed, namely, the higher the strain rate, the higher the maximum stress. Concerning the effects of the conditioning for PA6, RH0 specimens exhibited a rise of the maximum stresses of about 50%. The moisture conditioning had a more significant effect on the maximum stress than the strain rate. Combining an increase of strain rate and a decrease of the humidity resulted in more abrupt stress softening. This is clearly shown in Fig. 3a-right for PA6 by comparing the RH0 and RH50 tests results. After stress softening, a stress plateau was observed for all the tests, whatever the specimen geometry, microstructure or test conditions.

To better highlight the effects of the test conditions on the maximum stress, Fig. 3b illustrates all the test results (19 tests for PP and 11 tests for PA6). For PP, results obtained without any specific monitoring equipment are symbolized by black open circles. Red full circles are from tests equipped with a DC camera to record and measure the neck root radius ($R$) and the width $2a$ (see Fig. 4a). The blue square symbols correspond to the tests on samples observed at the ESRF. For PA6, the red open circles correspond to video recording and the blue open square symbols are tests involving ESRF tomography inspections.

Fig. 3b reveals the reproducibility of the stress-strain curves obtained by measuring the scatter on the maximum stress (Appendix B). It can be noted that a maximum scatter of 14% was observed for PP specimens tested at $d\varepsilon/dt = 10^{-3}\ s^{-1}$ (Fig. 3b-left).

Fig. 4a shows the shape of the necked region for each material. Qualitatively, a less whitened surface was observed around the mid-width region for the PP necked specimen (Fig. 4a-left). Actually, the net section sides underwent warping, leading to less deformed matter at the corners than that at mid-width and mid-thickness. For PA6 necked round bars, the axi-symmetry seems to have been well respected, resulting in homogeneity of the

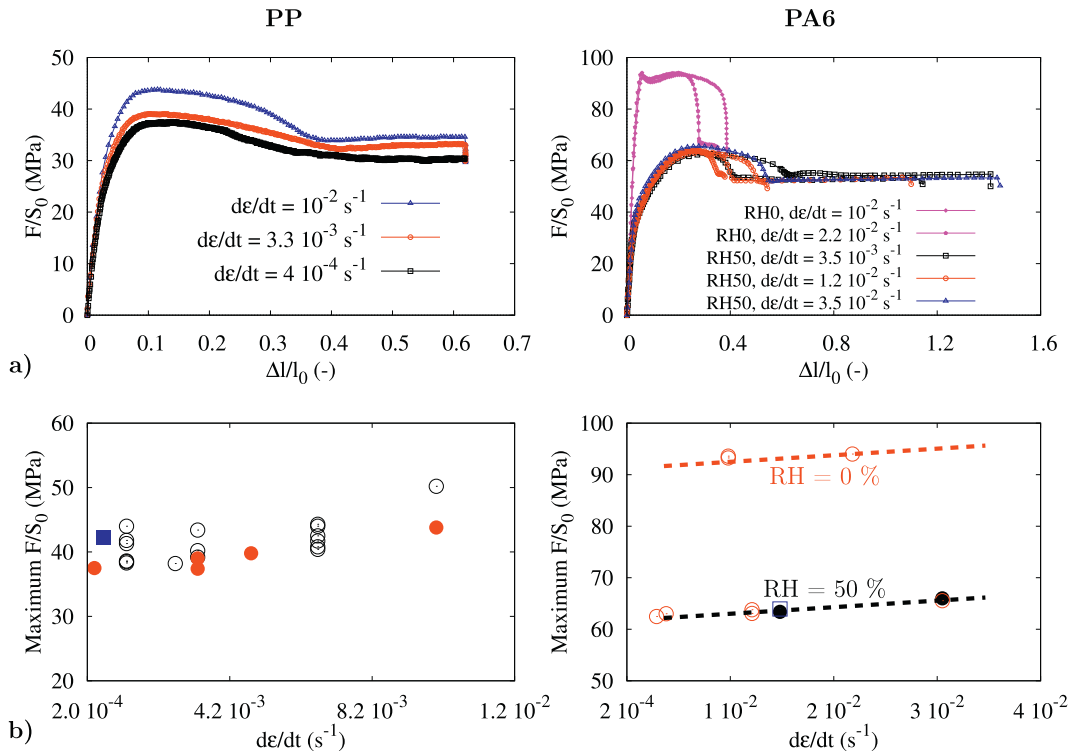


**Fig. 3.** Tensile test results for PP (left) and PA6 (right): a) Engineering stress-strain curves; b) Effects of the strain rate and the sample conditioning RH.

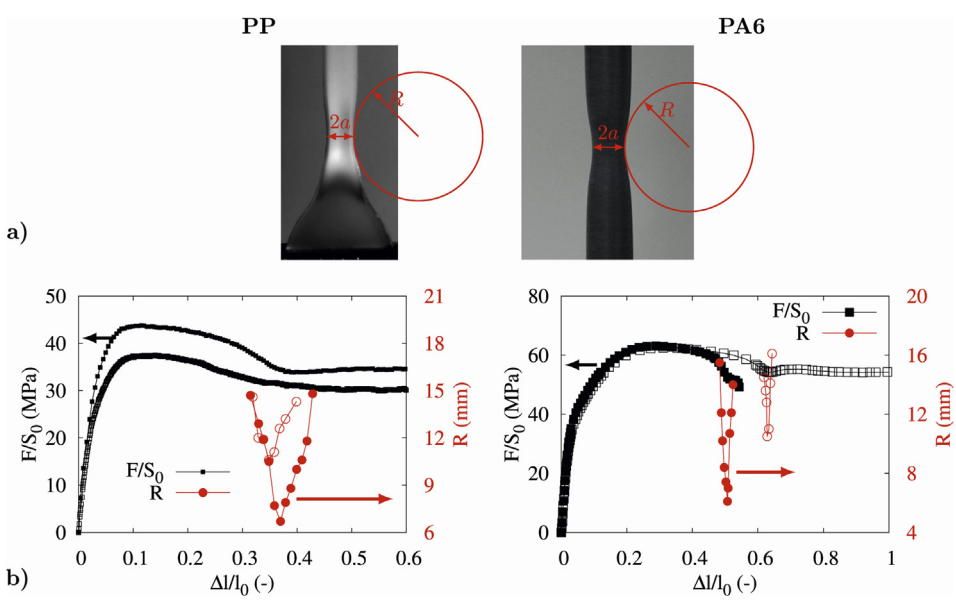


**Fig. 4.** Characterization of the necking region for PP (left) and PA6 (right): a) Definition of the minimal neck section (a) and curvature radii R; b) Measure of the engineering strain corresponding to the minimum curvature radius R. *Open symbols are for lower strain rates.*

deformation.

The definitions of the neck curvature radius ($R$) and the neck minimal section width "$a$" are recalled in Fig. 4a. Here, special attention was paid to the engineering strain corresponding to minimum $R$ values. These measured $R$-values have been superimposed on the stress-strain curves in Fig. 4b. For each material, two representative curves corresponding to two different strain rates have been plotted. The second $y$-axis of the diagram indicates the evolution of $R$ with respect to the applied engineering strain. It

**Table 3**
Engineering strain at the minimum neck curvature radius for PP material.

| Strain rate ($s^{-1}$) | Strain at minimum curvature radius (–) |
|---|---|
| $10^{-2}$ | 0.37 |
| $4.7\ 10^{-3}$ | 0.33 |
| $3.3\ 10^{-3}$ | 0.38 |
| $3.3\ 10^{-3}$ | 0.29 |
| $4\ 10^{-2}$ | 0.35 |

is clearly shown that the minimum neck curvature radius coincided with the end of stress softening. For all the tests where the *R* measurement was available, Tables 3 and 4 summarize the critical engineering strains corresponding to the minimum *R* for PP and PA6, respectively. It can be concluded that, whatever the material, the specimen geometry and the pre-conditioning, the engineering stress-strain curves showed a maximum stress, stress-softening and a plateau. The minimum curvature of the necking occurred systematically at the end of the stress-softening stage and corresponded to the beginning of the plateau.

**Table 4**
Engineering strain at the minimum neck curvature radius for PA6 material.

| Relative humidity (%) | Strain rate ($s^{-1}$) | Strain at minimum curvature radius (−) |
|---|---|---|
| RH0 | $10^{-2}$ | 0.36 |
| RH0 | $2.2\ 10^{-2}$ | 0.26 |
| RH50 | $3.5\ 10^{-3}$ | 0.63 |
| RH50 | $3.5\ 10^{-3}$ | 0.42 |
| RH50 | $1.2\ 10^{-2}$ | 0.51 |
| RH50 | $3.5\ 10^{-2}$ | 0.41 |
| RH50 | $2\ 10^{-2}$ | 0.35 |
| RH50 | $3.5\ 10^{-2}$ | 0.55 |

Fig. 5 shows significant results of the present work on the data of the neck curvature radii and the section of necked area. Fig. 5a plots the evolution of the transverse engineering strain defined as $\Delta a/a_0$, as a function of the axial engineering strain normalized by the strain at minimum curvature radius (Tables 3 and 4). A transition occurs just before the normalized strain equalled 1. Stabilization at about −40% and −50% of this transverse strain appeared for the normalized strain greater than 1 for the PP and PA6, respectively. These stabilized transverse strains can be compared with less that −10% measured in the remainder of the specimens. This clearly shows a gradient of the transverse deformation inside the necked

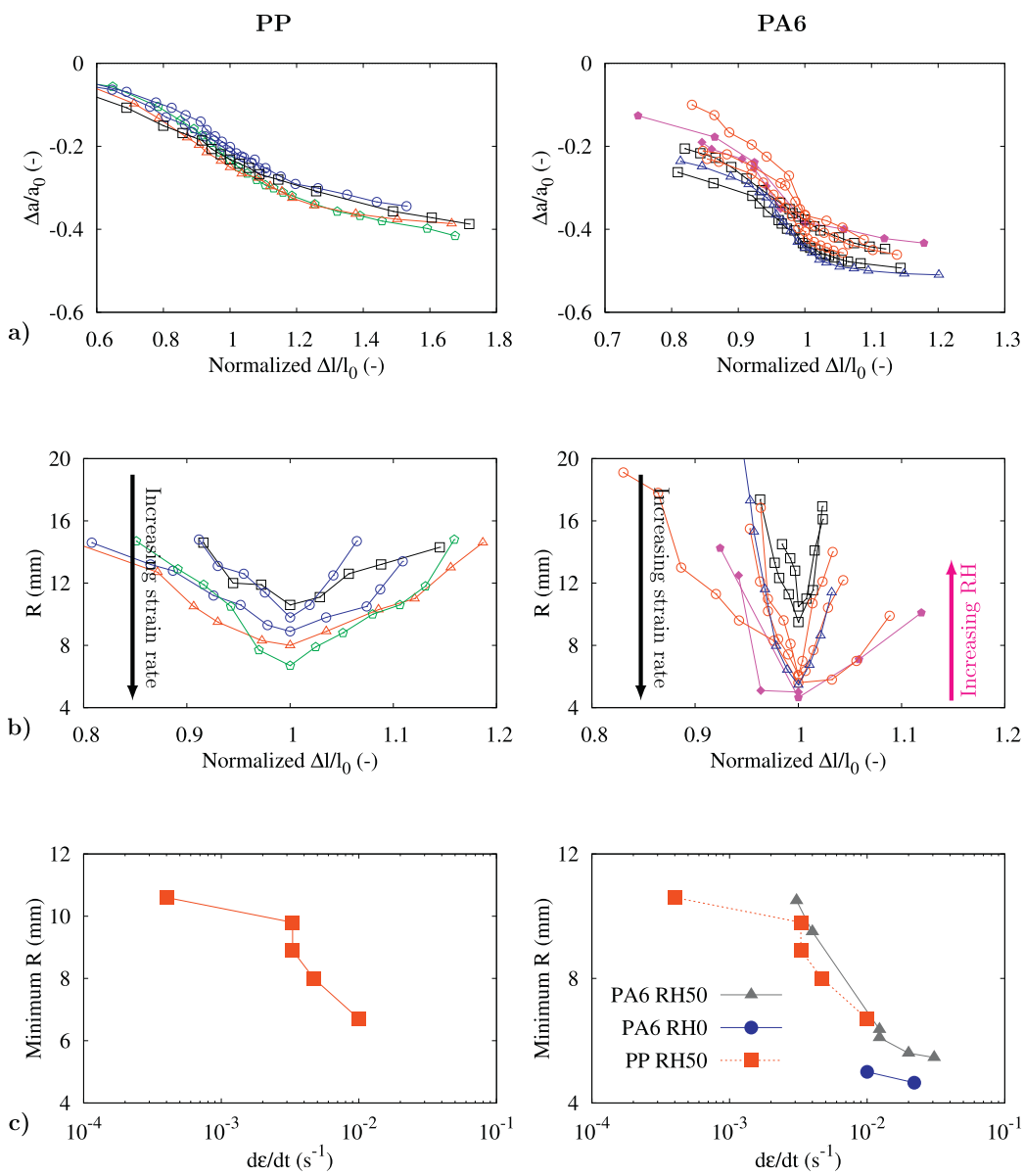


**Fig. 5.** Evolution of the characteristic lengths during the tests: a) Net section deformation $\Delta a/a_0$ *w.r.t.* the normalized engineering strain; b) Neck curvature radius R *w.r.t.* the normalized strain engineering; b) Minimum R *w.r.t.* the engineering strain rate.

specimen. Additionally, no effect of the strain rate was apparent, as shown in Fig. 5a. For the PP flat sample, measurements were carried out at both corners, which were presumed to correspond to minimum values, due to the warping of the sides of the section.

The evolution of $R$ around the normalized strain of 1 was analysed in Fig. 5b. Recall that $R$ begins with an infinite value (smooth specimens), its measurement was started at about 20 mm when the profile of the necking was well resolved. For the two materials, $R$ values decreased during the steep decrease in $\Delta a/a_0$, as shown in Fig. 5a. Then, when this latter stabilized (extension of the necking), $R$ increased asymptotically towards infinity again (blunting and extension of necked region). From Fig. 5b, $R$ minimum values were determined. Their ranges were estimated to be from 6 mm to 11 mm for PP and from 5 mm to 10 mm for PA6.

Fig. 5c shows the results of a detailed analysis of the effects of strain rate and pre-conditioning on the $R$ minimum values. For PP (Fig. 5c-left), the lower the strain rate, the higher the minimum $R$ value, presumably due to the viscous flow of the material. These results were obtained for a plate specimen exhibiting skin-core effects where the necking could be measured by observing changes in the specimen's width. The thickness change in shape was not measured. For PA6 round bars (Fig. 5c-right), the same trends as for PP were observed for the strain rate effects. The influence of conditioning (RH) was further highlighted (full circles in the bottom of Fig. 5c-right): a decrease in RH resulted in a decrease in the $R$ minimum value, similar to an increase of strain rate.

When the results for PP were superimposed in Fig. 5c-right (red squares), it was noticed that for $d\varepsilon/dt > 2\ 10^{-3}\ s^{-1}$ the two materials exhibited the same values of minimum $R$.

### 4.2. Tomography results

The necked regions of the two materials were inspected by SRCT with 0.7 μm resolution. The analysis proposed here first identified the arrangement of clusters of voids as "polar fans" [22], then quantified the heights and the orientations of these polar fans along the axial and radial directions.

#### 4.2.1. Polar fans

Fig. 6 shows an overview of the scans for the deformed PP samples corresponding to Fig. 1b-left. Top views are presented on the left side of the figure whereas through thickness side views are shown on the right side. The loading direction corresponding to the $z$-axis is illustrated by the cylindrical coordinates at the bottom of Fig. 6.

From the top views, the whole thickness of the sample bounded by the curved lines representing the surfaces can be seen. These curved lines clearly show the warping of the sides of the sections, as indicated in the top-left picture of Fig 6. This confirms that the section was no longer rectangular due to a heterogeneous deformation. Within the thickness, the skin and the core can be distinguished (arrows and comments in yellow). Circular voids are visible in the core, presumably because they were well resolved. The core section remained rectangular during the deformation. Therefore, for the PP which initially exhibited a skin-core effect, the core seems to have deformed homogeneously whereas the skin underwent heterogeneous deformation.

The side views, cut at mid-width, clearly reveal the shape of the necked sample through the thickness. Similar to the neck curvature radii measured at both sides of the width, a neck curvature radius through the thickness can be estimated in the top right view. This allows the assumption of isotropy to be checked. The thickness varies along the $z$-axis, the minimum value being located in the top right side view and the maximum at the bottom. A heterogeneous deformation along the load direction ($z$-axis) can then be concluded.

The skin-core microstructure can also be noticed all along these side views. In the core, voids can be observed as vertical black stripes separated by "white" matter. These stripes were identified as polar fans. One example of polar fans is surrounded by a yellow dashed line in the top right view of Fig. 6. Furthermore, some deformed spherulites are visible, especially at the interface between the skin and the core.

The paths used to plot the characteristic parameters of the microstructure are defined in Fig 6. They are illustrated by three dashed arrows labelled as: i) inside the neck; ii) outside the neck; iii) axial, in the loading direction. Note that there is a gap between the two top blocks inducing a discontinuity in the distribution with respect to the $z$-axis.

Similar to PP, Fig. 7 shows an overview of the scans of a PA6 sample having undergone necking (Fig. 2b-right). Only side views are presented here. The load direction was vertical as illustrated by the orientation of cylindrical coordinates depicted at the bottom of Fig. 7. The dashed line added on the left side of the figure indicates the free surface of the specimen showing the profile of the necking zone. A series of scans was carried out following two radial and one axial path indicated in this figure. The radial paths were selected, respectively, inside the neck and outside the neck regions.

As expected, no skin-core effects on the microstructure were observed here. At this scale, polar fans seen as vertical black stripes can also be observed. An example is illustrated within the yellow ellipse in the top part of the figure. The "density" of polar fans was a maximum in the central part of the necking zone (top left images). Some artefacts appeared in two of the reconstructed volumes in the vicinity of the surface of neck shoulder.

Quantification of characteristic lengths requires first a description of the observed microstructures with a clear definition of the pattern to which the measurement is applied. Unlike many works dealing with individual voids, the focus here is on the microstructures of polar fans seen in several semi-crystalline polymers subjected locally to a moderate stress triaxiality ratio [19], including uniaxial tensile stress but generally when the specimen has undergone necking [6,23,24]. Polar fans consist of a cluster of voids aligned in columns in the loading direction (poles) that are separated by walls within a spherulite. The fans converge to the centre of the spherulite such that the two voids closest to the centre are conical shaped. Elsewhere, they are cylindrical and separated by disk shaped walls of matter. The polar fans are constituted of two fans that will be noted as south and north fans, respectively, according to whether there is divergence from the centre to the south or the north pole of the spherulite. A longitudinal cut of an idealized polar fan would give symmetrical images of voids aligned in columns with respect to the centre of the spherulite.

The salient observations of the polar fans structures are detailed in Fig. 8.

Fig. 8a illustrates two "ideal" polar fans for the PP. The dashed yellow line indicates approximately the boundary of the spherulite. For the PP, voids (in black) have more complex morphology (zigzag) than the cylindrical/conical shape mentioned above. The south polar fan seems to have a smaller diameter, presumably due to an out of plane tilt. This is the basic pattern allowing the selection of polar fans as well as the measurement of their characteristic parameters, such as their total height and orientation, the number of voids within a fan, the maximum height and diameter of voids inside a fan.

For the PA6 material, Fig. 8b shows polar fans selected from the central part of the necked zone. Triple polar fans were encountered especially in this region. It can be observed that the walls (matter separating voids) were rather straight in comparison to the PP fans. Moreover, at this stage of local deformation, coalescence in column

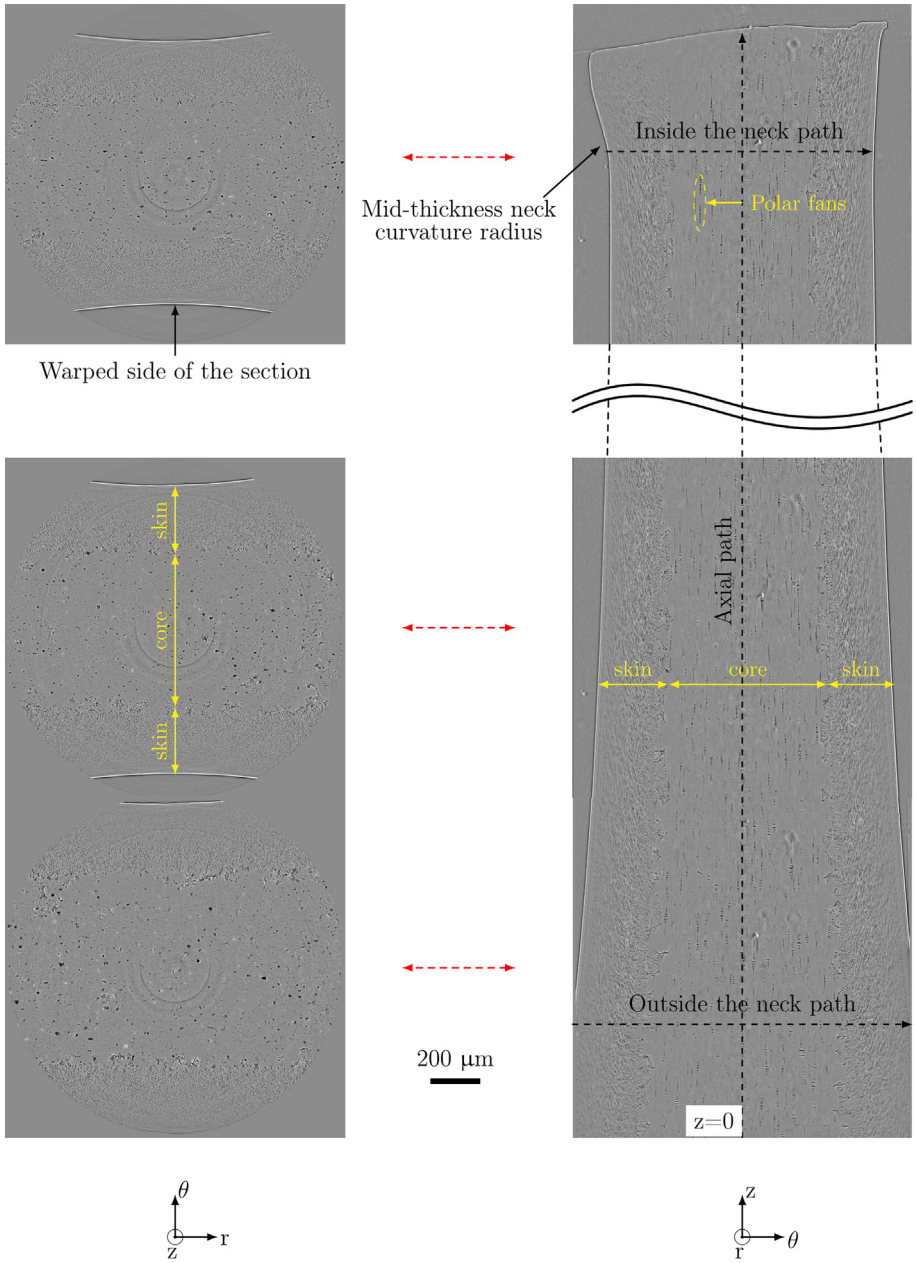


**Fig. 6.** PP microstructure: overview of tomographic volumes.

of voids can be seen to have occurred. This induced both a decrease in the number of voids and an increase in the maximum height of voids within a given fan.

Fig. 8c depicts twin polar fans in the PP also. They have been observed in the minimum thickness region submitted to higher deformation. Accordingly, the north fan exhibits straight walls, presumably due to radial coalescence of voids from a radial neighbouring fan. The maximum diameter of voids within this fan was, therefore, doubled.

Fig. 8d shows results from the PA6 specimens and highlights two kinds of coalescence: i) coalescence in a column from two concomitant north/south fans, merging the two extreme voids of both fans; ii) radial coalescence of aligned voids from twin fans. Their consequence was an increase in the number of voids within the coalesced fans and, as mentioned above, an increase in the maximum diameter of void within a fan.

Fig. 8e shows a specific observation for the PP due to the skin-core effects of the microstructure. Indeed, at the interface, a large spherulitic microstructure is clearly discernible in the core, whereas no specific feature was observed in the left half part in the skin. These quasi-parabolic spherulites - called also “comets” [15,16,25,26] (Fig. 2a) – are prone to develop equatorial void nucleation and growth due to the separation of horizontal crystalline lamellae.

For the PA6 specimens, the volume examined near the surface at the neck shoulder (end of the outside the neck path in Fig. 7) showed oriented polar fans following the inclination of the free surface. Fig. 8f highlights such observations where the approximate boundary of the spherulite has been delineated by the dashed red line. The inclined north fan is clearly visible whereas, for the south fan, only the void corresponding to the end is observable. Furthermore, in this spherulite, equatorial voids were clearly discerned. This configuration allowed the definition of the tilt angle to be given. It was also observed that, despite the general inclination

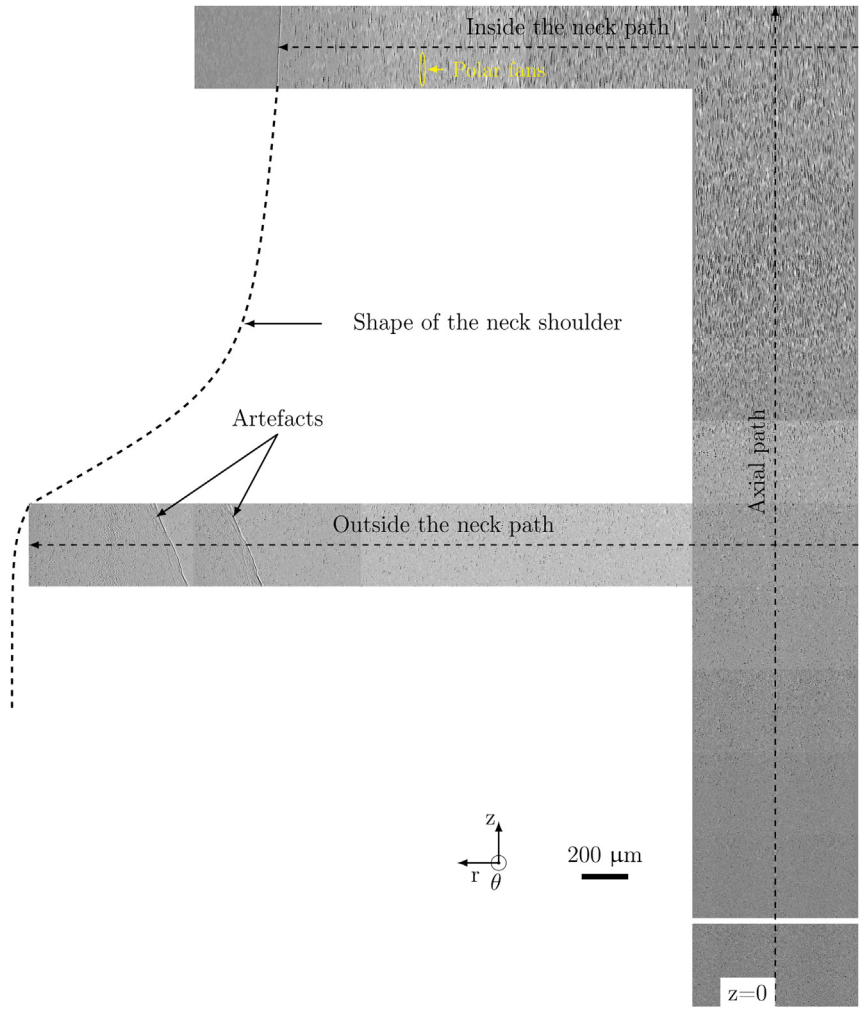


**Fig. 7.** PA6 microstructure: overview of tomographic volumes.

of the fans, the individual voids seem to have remained perpendicular to the loading direction. This would mean that the spherulite was sheared after the nucleation of the polar fans.

*4.2.2. Characteristic measurements performed on polar fans*

Once the structures of the polar fans were identified, data processing was performed on the following characteristic parameters of the polar fans:

- the total height of the polar fans in the side view, giving an estimate of the height of the spherulite;
- the in-plane tilt of the polar fans given by the angle between a vertical line (z-axis) and the global orientation of the polar fans (Fig. 8f);
- the maximum height of voids within the fans, giving an order of magnitude of their axial strains;
- the maximum diameter of voids within the fans corresponding to their radial strains;
- the number of voids within a fan allowing the inter-voids or inter-fans coalescences in column to be analysed.

The axial distributions of polar fans and maximum void heights are depicted in Fig. 9. The z abscissas of the plots, starting from the points noted as "$z = 0$", are shown in Figs. 6–7 and labelled as "axial paths" for PP and PA6 respectively.

For the PP (Fig. 9 left), the average heights of the maximum void and polar fans differed by about one decade (about 5 µm and 100 µm, respectively). Moreover, since the thickness of the PP had a smooth increase (Fig. 6), only a small slope of the height evolution was observed. Conversely, for PA6 (Fig. 9 right) the increase in heights of both parameters was more significant. The transition was located between 3 mm and 5 mm through the neck shoulder. The mean height of polar fans evolved from 20 µm, in the outside of the striction region, to 100 µm within the necked area. This allows an estimate of about 400% axial large strain undergone by spherulites during the necking process. For the maximum void height (located near the poles), the evolution ranged from 2 µm to 15 µm approximately, yielding 650% axial strain. However, the axial strain of each void was observed to significantly vary depending on its location in the structures of the polar fans. Indeed, conical voids near the spherulite centre were less deformed axially. Furthermore, the deformation of the matrix in the central region of the spherulite could be observed through the increasing distance between these two conical voids (see for instance Fig. 8a). The overall deformation of the spherulite in the load direction consisted then of volumetric deformation relative to void growth and an extension of the matrix. These deformations within the spherulite were extremely heterogeneous both in nature and in value.

Fig. 10 depicts the radial distributions of the polar fans' tilt angle and height. The $r$ abscissas of the plots are shown in Figs. 6–7.

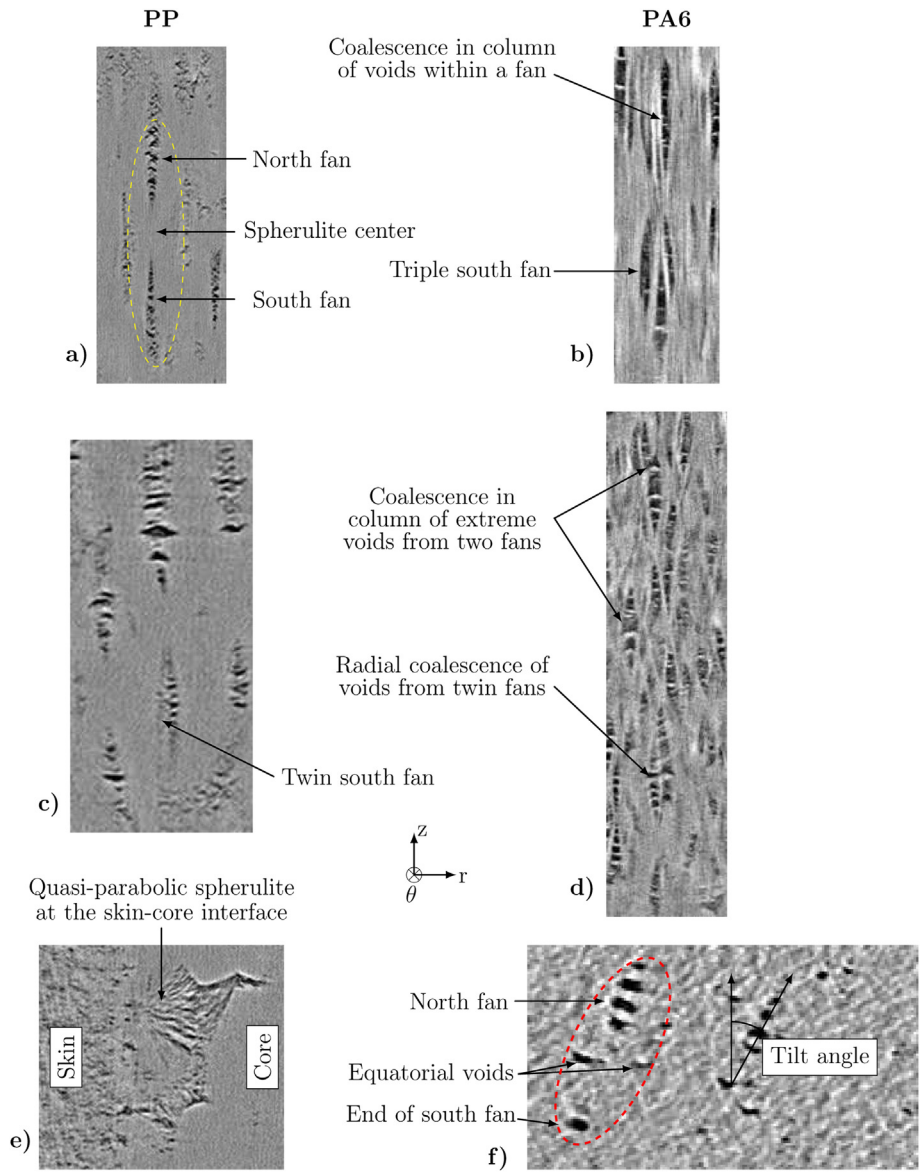


**Fig. 8.** Polar Fan structures: Left PP; Right PA6. a)–c) Various aspects of polar fan microstructures; d) Radial and axial coalescences of voids in polar fans due to external deformation; e) Deformed spherulite at the interface of the skin and core in PP; f) Tilt angle for polar fans located near the neck shoulder.

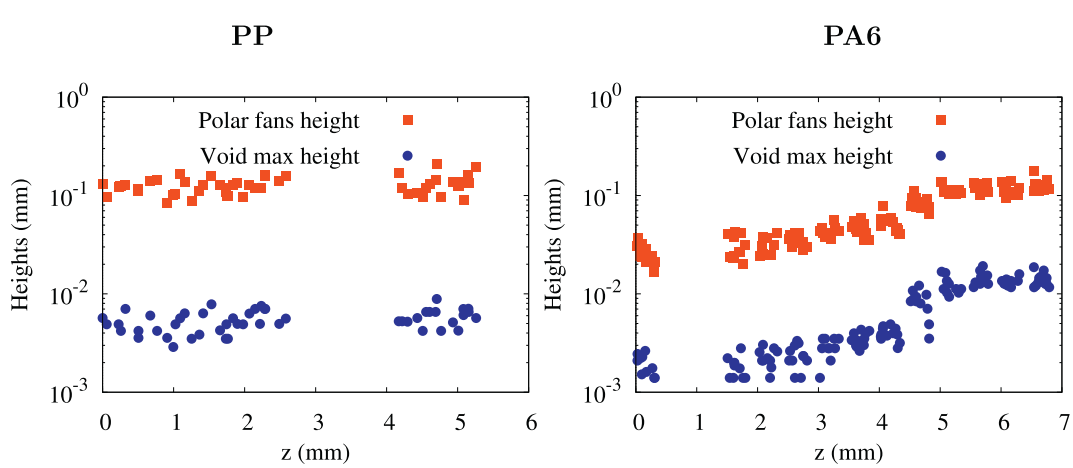


**Fig. 9.** Axial evolution of polar fans and void heights: left for PP and right for PA6.

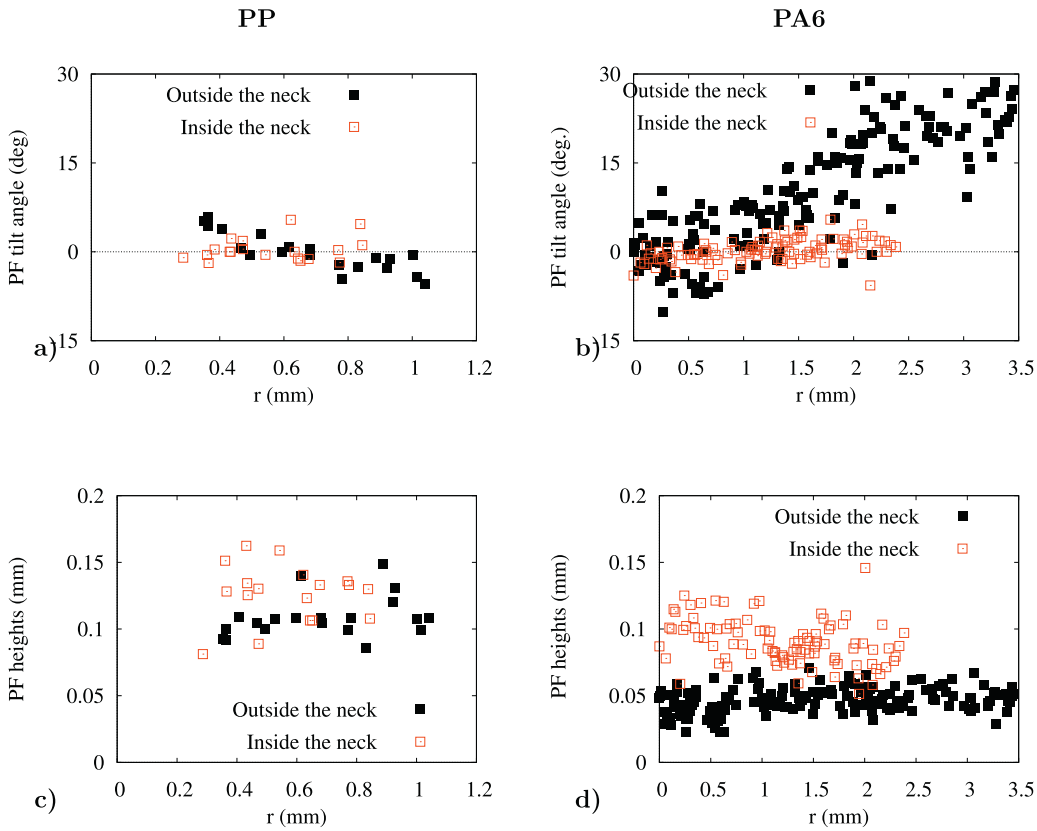


**Fig. 10.** Radial evolution of a-b) PF orientation, c-d) PF height. (PF = polar fans).

Dashed arrows, labelled as "Inside the neck path" (open square symbols) and "Outside the neck path" (full square symbols) for each polymer characterize the paths where *r* was measured. The origins of the paths corresponding to the starting points of the arrows were related to some borders of the tomographic images. Actually, the exact location of the centre of the PA6 specimen was unknown. This is the practical reason for the choice of the above mentioned origins. Moreover, the "Outside the neck paths" were not completely outside of the necked region. It can be clearly seen in Fig. 6 for PP, that the thickness still increased in a downwards direction. The plots are presented with the same polar fans' height-scale so as to analyze comparatively the two materials. The heights and tilt angles of the polar fans were measured in the core part for PP and within the whole section radius for PA6.

The first parameter to be studied was the in-plane tilt of the polar fans. It should be recalled that, in Fig. 8f, a qualitative description of this inclination was given so as to define the tilt angle measured between a vertical line (*z*-axis) and the global orientation of the polar fans. A tilt angle of 0° means that the polar fans were aligned along the load direction. This is the case inside the necked region, as clearly observed in Fig. 10a–b (open square symbols). For both materials, the scatter was estimated at ± 3°.The situation was drastically different in the outside region of the neck section, corresponding to the neck shoulders. For the PP, in the core region the tilt angle evolved from 5° to −5° side to side. The gradient was not so pronounced because of the smooth evolution of the thickness with respect to *z*-axis. It should be recalled that the tilt angle tended to follow the outer surface inclination [18]. For the PA6, the gradient of the tilt angle was more significant, ranging from 0° to 30° through the section radius. This orientation of the polar fans has already been reported for tests conducted on PA6 axisymmetrically notched specimens for moderate stress triaxiality [18]. These results highlight heterogeneity in the tilt angle within the section of the specimen. This was not taken into account when calculating the true strain.

The measurement now considers the heights of the polar fans. Fig. 10c shows that for the PP, the average height of the polar fans was about 100 μm with a scatter around 60 μm. In spite of this large scatter, it can be noticed that, within the necked region, the average height was 20 μm higher than that observed in the out of neck path. As mentioned above, the width of the region of interest was about 0.8 mm, corresponding to the core alone. The deformation of the spherulites in this region was homogeneous. No information about the skin was available.

For the PA6 material, Fig. 10d reveals a larger span of the region of interest: 3.5 mm. Outside the necking zone, heights of the polar fans were constant in the section, having an average value of about 50 μm. The deformation of the spherulites was homogeneous. Inside the necking region, the radial distribution of the heights of the polar fans (open square symbol) showed a gradient, the maximum of which was located in the central part of the specimen with an average height of about 100 μm. The minimum average height located at the surface (neck root radius) was estimated at 70 μm. This is in agreement with the stress profiles predicted by Bridgman's formulae [8] denoting a multiaxial stress state and volumetric strain.

Fig. 11 displays the radial evolutions of the maximum void diameter. The void under consideration was chosen as having the maximum diameter amongst those inside the polar fans. It can be seen for PP (Fig. 11a) that there was a significant scatter, but the average line of voids inside the neck was lower than that of the ones outside the neck. This indicates that the necking led to a shrinkage in diameter of the penny shaped voids [7]. For the PA6 (Fig. 11b), the magnitude of the scatter was smaller than that of the PP. Maximum

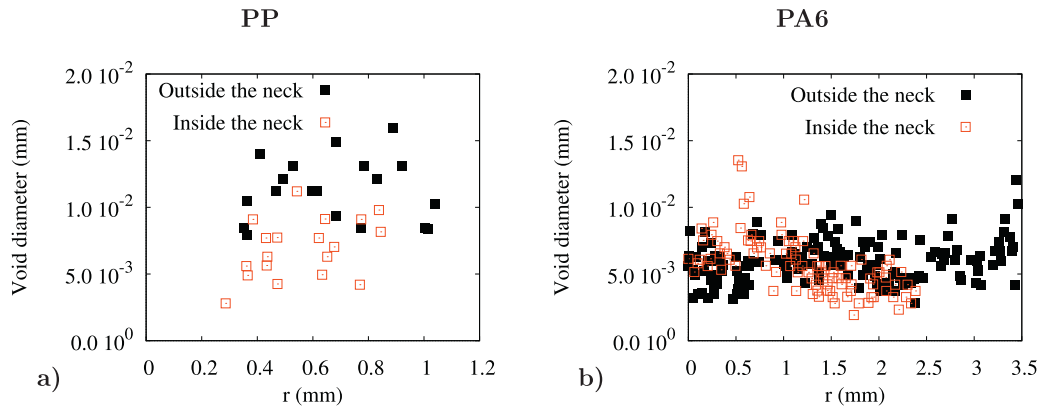


**Fig. 11.** Radial evolution of void diameter.

voids outside the neck had an average diameter of 5 μm. Inside the necked section, a gradient of the diameter can be observed, the average value of which is a maximum in the centre of the section (about 7 μm) and minimum at the surface (about 3 μm).

## 5. Discussion

### 5.1. Experimental measurements

The usual experimental data are measured in the outer surfaces of the specimens. Even full field extensometry using digital image correlation (DIC) would be limited to the observation of the external surface. In the present work, tomographic images allow the observation of the warping of sides from an initial rectangular section, showing heterogeneous out of plane deformation. Thus, a homogeneous correction of the out of plane strain in the DIC software is presumably not sufficient. Furthermore, it demonstrates that the extension of the surface measurements into 3D through the thickness interpretations is problematic. Indeed, even for an initially homogeneous (micro)structure like those of PA6, heterogeneity of characteristic lengths was revealed at the onset of the necking. This heterogeneity increased for flat specimens exhibiting an initial skin-core effect, similar to the PP samples here.

The load cell in a tensile test indicates the resulting overall macroscopic force applied to the specimens. This global measure is currently assumed to be homogeneously distributed throughout the net section, giving the engineering stress. However, as soon as a necking appears during the test, the localization induces transverse stresses [8]. In this case, the stress state inside the necked section is neither homogeneous nor uniaxial.

### 5.2. Local estimations of the strains

The deformation could be assessed using some characteristic lengths within the microstructure. The 3D and through thickness data provided in the present work allowed a measure to be made of the heterogeneity of the void and polar fans' heights and diameters. The corresponding deformations could then be estimated from Fig. 10d measurements on the deformed polar fans, yielding the axial engineering strain gradient within the net section. In the central part, the calculation led to a deformation of the polar fans of about $\varepsilon_z \approx 100\%$ whereas at the surface $\varepsilon_z \approx 40\%$. These results highlight the heterogeneity of the axial deformation inside the neck. Furthermore, the abscissa of Fig. 10d allows an estimate of the average radial deformation $\varepsilon_r$. Indeed, the section radius decreases from 3.5 mm (outside the neck) to 2.5 mm (inside the neck). This yields an approximate radial engineering strain of about $\varepsilon_r \approx$ -30%. If the radial deformation is assumed to be homogeneous in the section [8], the volume change can be calculated as the sum of the three principal strains: $\Delta V/V_0 = \varepsilon_z + 2\ \varepsilon_r$. This yields volume changes of +40% in the bulk and −20% at the surface where usually measurements are carried out. The zero volume change (incompressible) is located somewhere in between the centre and the outer surface of the section. The overall volume change within the section was also heterogeneous [7]. This makes questionable the estimation of the volume change by assuming homogeneous extension of the measurement at the surface [1,10–13].

The overall volume change mentioned above has been estimated for the matrix combined with the voids. A local estimate of the volume variation due exclusively to void growth could be attempted from Figs. 11b and 9b. Indeed, Fig. 11b depicting the evolution of maximum void diameter permits evaluation of an increase of about 40% in void diameter in the central part, as well as a decrease of about −40% in the vicinity of the necked surface. Combined with the evolution of the void height in Fig. 9b, these latter data allow an estimation of the pure volume change of voids within the material. It should be recalled that $\varepsilon_z \approx 650\%$, void growth measurements indicate values as high as 730% in the centre and 570% near the surface.

### 5.3. Consequences for the constitutive modelling approaches

A constitutive model enables the relationship between the true stress tensor and the true strain tensor to be described. The results obtained in the present paper have raised discussion about to what extent these observations affect the mechanical response of a given material. The high values of void growth observed here imply, on the one hand, a need for finite strain formulations; on the other hand, that corrections to the net section should be made that would significantly increase the true stress. For instance, at the normalized strain equal to unity (Fig. 5), the stress-strain curve should be corrected by using, at least, the triaxiality correction [13]. To better analyze the effects of voiding, the stress and strain tensors should be split into their deviatoric and hydrostatic parts. Current constitutive models are essentially based on the relationship between the deviatoric stress (Von Mises) and the deviatoric strain (shear). The relationship between the hydrostatic pressure and the volumetric strain (void growth) needs further data. Tests on notched specimens allow this aspect to be studied [7,18].

## 6. Conclusions

PP and PA6 semi-crystalline polymers were submitted to tensile tests at 20 °C, with pre-conditioning and strain rates selected to

provoke necking of the specimens. In contrast to the usually measured parameters, such as load and extension, the experimental data collected also included information on through thickness deformation in 3D. The influence of the geometry has been studied: the PP specimens were flat and the microstructure showed a skin-core structure whereas the PA6 specimens were homogeneous round bars taken from the core of a thick plate. During the deformation, the external sides of the PP rectangular section became curved (warped). Nevertheless, the core part remained rectangular. The PA6 round bars stayed axi-symmetric during the extension. This geometry is easier to model due to its ideally homogenized deformation.

The main outcomes of the study concern new experimental methods to collect specific data at the macroscopic scale (surface measurement of the necking) and at the microscopic scale underneath (void of polar fans height and diameter). The results can be summarized as follows:

- The necking process consists of a gradual localization of the deformation at a given site within the gauge length. It involves a decrease in both the net section area and the neck curvature radius. The minimum neck curvature radius was systematically reached at the end of the post-yielding stress softening. Its value, ranging from 5 mm to 10 mm for the two materials, decreased as the strain rate increased and as the relative humidity decreased.
- At the microstructural scale, a 3D and through thickness study of polar fans was carried out in terms of morphology and general arrangement. The axial and radial distributions of the height, the in-plane tilt angle, the maximum void height and diameter of the polar fans were then plotted. The impact of the void growth and coalescence on the deformation of the spherulites was highlighted. Large volumetric strains (volume change) as high as 100% were induced by these microstructural evolutions. Non homogeneous distribution of the strain tensor was demonstrated. Therefore, a measurement of volume variations at the surface could be erroneous.

In terms of finite element analysis, it is recommended to use finite strain formulations and to enrich the usual uniaxial tensile tests results with further data so as to better assess constitutive models dedicated to complex engineering structures submitted to multiaxial stress states.

## Acknowledgment

The authors thank Anthony Bunsell for scientific discussions, Julie Heurtel and Stéphanie Dang for technical help. ESRF is greatly acknowledged for beam time in experiment MA1267.

## Appendix A. Supplementary data

Supplementary data related to this article can be found at http://dx.doi.org/10.1016/j.polymertesting.2016.09.012.

## References

[1] C. G'sell, J.M. Hiver, A. Dahoun, Experimental characterization of deformation damage in solid polymers under tension and its interrelation with necking, Int. J. Solids Struct. 39 (2002) 3857–3872.
[2] B. Xiong, O. Lame, J.M. Chenal, C. Rochas, R. Séguéla, G. Vigier, In-situ SAXS study and modeling of cavitation/crystal-shear competition in semi-crystalline polymers: influence of temperature and microstructure in polyethylene, Polymer 54 (2013) 5408–5418.
[3] T.F. Morgeneyer, H. Proudhon, P. Cloetens, W. Ludwig, Q. Roirand, L. Laiarinandrasana, E. Maire, Nanovoid morphology and distribution in deformed HDPE studied by magnified synchrotron radiation holotomography, Polymer 55 (2014) 6439–6443.
[4] L. Farge, S. André, P. Pawlak, C. Baravian, S. Irvine, A. Philippe, A study of the deformation induced whitening phenomenon for cavitating and non-cavitating semicrystalline polymers, J. Polym. Sci. Part B Polym. Phys. 51 (2013) 826–841.
[5] N. Brusselle-Dupend, E. Rosenberg, J. Adrien, Characterization of cavitation development while tensile testing PVF2 using 3-D X-ray microtomography, J. Mater. Sci. Eng. A 530 (2011) 36–50.
[6] L. Laiarinandrasana, T. Morgeneyer, H. Proudhon, C. Regrain, Damage of semicrystalline polyamide 6 assessed by 3D X-ray tomography: from microstructural evolution to constitutive modeling, J. Polym. Sci. Part B Polym. Phys. 48 (2010) 1516–1525.
[7] L. Laiarinandrasana, O. Klinkova, T.F. Morgeneyer, H. Proudhon, F. Nguyen, W. Ludwig, Three dimensional quantification of anisotropic void evolution in deformed semi-crystalline polyamide 6, Int. J. Plast. 83 (2016) 19–36.
[8] P. Bridgman, The stress distribution at the neck of a tension specimen, Trans. ASME 32 (1944) 553–574.
[9] G. Boisot, L. Laiarinandrasana, J. Besson, C. Fond, G. Hochstetter, Experimental investigations and modeling of volume change induced by void growth in polyamide 11, Int. J. Solids Struct. 48 (2011) 2642–2654.
[10] V. Gaucher-Miri, C. Depecker, R. Séguéla, Reversible strain-induced order in the amorphous phase of a low-density ehylene/butene copolymer, J. Polym. Sci. Part B Polym. Phys. 35 (1997) 2151–2159.
[11] L. Cangemi, S. Elkoun, C. G'Sell, Y. Meimon, Volume strain changes of plasticized poly(vinylidene fluoride) during tensile and creep tests, J. Appl. Polym. Sci. 91 (2004) 1784–1791.
[12] F. Addiego, A. Dahoun, C. G'Sell, J.M. Hiver, Characterization of volume strain at large deformation under uniaxial tension in high-density polyethylene, Polymer 47 (2006) 4387–4399.
[13] M. Ponçot, F. Addiego, A. Dahoun, True intrinsic mechanical behaviour of semi-crystalline and amorphous polymers: influences of volume deformation and cavities shape, Int. J. Plast. 40 (2013) 126–139.
[14] F.M. Beremin, Elastoplastic calculation of circumferentially notched specimens using the finite element method, J. Mec. App. 4 (1980) 307–325.
[15] J.M. Haudin, Handbook of Polymer Crystallization, John Wiley & Sons, Inc., Hoboken: New Jersey, USA Dunod, 2013. E. Piorkowska et G.C. Rutledge.
[16] A. Lovinger, C. Gryte, Model for the shape of polymer spherulites formed in a temperature gradient, J. Appl. Phys. 47 (5) (1976) 1999–2004.
[17] C. Regrain, L. Laiarinandrasana, S. Toillon, K. Saï, Multi-mechanism models for semi-crystalline polymer: constitutive relations and finite element implementation, Int. J. Plast. 25 (2009) 1253–1279.
[18] H.A. Cayzac, K. Saï, L. Laiarinandrasana, Damage based constitutive relationships in semi-crystalline polymer by using multi-mechanisms model, Int. J. Plast. 51 (2013) 47–64.
[19] L. Laiarinandrasana, T. Morgeneyer, H. Proudhon, F. N'Guyen, E. Maire, Effect of multiaxial stress state on morphology and spatial distribution of voids in deformed semicrystalline polymer assessed by X-ray tomography, Macromolecules 45 (2012) 4658–4668.
[20] P.A. Douissard, A. Cecilia, X. Rochet, X. Chapel, T. Martin, T. van de Kamp, L. Helfen, T. Baumbach, L. Luquot, X. Xiao, J. Meinhardt, A. Rack, A versatile indirect detector design for hard X-ray microimaging, J. Instrum. 7 (9) (2012) P09016.
[21] S. Chilingaryan, A. Mirone, A. Hammersley, C. Ferrero, L. Helfen, A. Kopmann, T. dos Santos Rolo, P. Vagovic, A GPU-based architecture for real-time data assessment at synchrotron experiments, IEEE Trans. Nucl. Sci. 58 (2011) 1447–1455.
[22] A. Rozanski, A. Galeski, Plastic yielding of semicrystalline polymers affected by amorphous phase, Int. J. Plast. 41 (2013) 14–29.
[23] A. Pawlak, A. Galeski, Cavitation during tensile deformation of polypropylene, Macromolecules 41 (2008) 2839–2851.
[24] A. Pawlak, A. Galeski, Cavitation and morphological changes in Polypropylene deformed at elevated temperatures, J. Polym. Sci. Part B Polym. Phys. 48 (2010) 1271–1280.
[25] A. Ibhadon, Fracture mechanics of polypropylene: effect of molecular characteristics, crystallization conditions, and annealing on morphology and impact performance, J. Appl. Polym. Sci. 69 (1998) 2657–2661.
[26] L. Norton, A. Keller, The scherulitic and lamellar morphology of melt crystallized isostatic polypropylene, Polymer 26 (1985) 704–716.